

A Model for the Complete Radial Structure of the Tropical Cyclone Wind Field. Part I: Comparison with Observed Structure*

DANIEL R. CHAVAS AND NING LIN

Princeton University, Princeton, New Jersey

KERRY EMANUEL

Massachusetts Institute of Technology, Cambridge, Massachusetts

(Manuscript received 5 December 2014, in final form 12 June 2015)

ABSTRACT

Part I of this work develops a simple model for the complete radial structure of the low-level tropical cyclone wind field. The model is constructed by mathematically merging existing theoretical solutions for the radial wind structure at the top of the boundary layer in the inner ascending and outer descending regions. The model is then compared with two observational datasets. First, the outer solution is compared with a global database from the QuikSCAT satellite (1999–2009) and found to reproduce the characteristic wind structure of the broad outer region of tropical cyclones at large radii, indicating that the solution successfully captures the physics of this region. Second, the inner solution is compared with the HWind database (2004–12) for the Atlantic and eastern Pacific basins and is shown to be capable of reproducing the inner-core structure while substantially underestimating wind speeds at larger radii. The complete model is then shown to largely, though not entirely, rectify this underestimation. Limitations of the model are discussed, including the need for a formal evaluation of the physics of the inner core as well as a transition-region model at intermediate radii characterized by intermittent convection, such as spiral rainbands. Part II will characterize the model's modes of wind field variability and their relationship to the variability observed in nature.

1. Introduction

Theoretical solutions for key aspects of tropical cyclone behavior have been demonstrated to successfully explain observations of real storms in nature. The upper bound on storm peak wind speed is credibly captured by potential intensity (PI) theory (Emanuel 2000; DeMaria and Kaplan 1994). Time-dependent changes in storm intensity are described well by ventilation-modified PI theory (Tang

and Emanuel 2012), which provides a solution for the dependence of both peak intensity and intensification rate on the combined effects of wind shear and dry air. The wide variation of overall storm size in nature (Merrill 1984; Chavas and Emanuel 2010; Knaff et al. 2014) is arguably an implicit prediction of PI theory, which is defined in terms of relative changes in angular momentum with radius while remaining agnostic to any specific absolute angular momentum value; the theory further predicts an upper bound on size, given by the ratio of PI to the Coriolis parameter, that is consistent with observations. Finally, storm motion in the tropics is accurately reproduced by beta-and-advection theory (Holland 1984).

Comparably little attention has been given to the physics underlying the radial structure of a tropical cyclone, despite the acknowledged sensitivity of wind and storm surge hazards and the economic damages they inflict to this storm characteristic (Lin and Chavas 2012; Irish and Resio 2010; Czajkowski and Done 2014; Chavas et al. 2013). Indeed, most existing models for radial structure used in practical applications are partially

 Denotes Open Access content.

* Supplemental information related to this paper is available at the Journals Online website: <http://dx.doi.org/10.1175/JAS-D-15-0014.s1>.

Corresponding author address: Daniel R. Chavas, Department of Civil and Environmental Engineering, Princeton University, E-316 E-Quad, Princeton, NJ 08544.
E-mail: drchavas@gmail.com

DOI: 10.1175/JAS-D-15-0014.1

empirical (Holland 1980; Holland et al. 2010; Jelesnianski 1966). Nonetheless, theoretical solutions for radial wind structure do exist. Emanuel (2004) derived models for the outer nonconvecting region where convection is absent, based on the combination of free-tropospheric thermodynamic balance and boundary layer Ekman dynamic balance, and for the inner convecting region, based on boundary layer angular momentum balance and entropy quasi equilibrium; these solutions were then asymptotically merged. More recently, Emanuel and Rotunno (2011) derived an improved solution for the inner region that arises from stratification of the outflow due to Kelvin–Helmholtz turbulence generated by the storm itself, which imposes a radial gradient in convective outflow temperature and, in turn, wind speed at the top of the boundary layer. In particular, this inner-region solution and the outer-region solution of Emanuel (2004) have each been shown to be useful for predicting storm structure in an idealized axisymmetric modeling environment (Emanuel and Rotunno 2011; Chavas and Emanuel 2014).

However, the ability of these theories to explain radial wind structure in observations is currently unexplored. Past observational studies indicate that the inner-core circulation appears to evolve nearly independently of the outer circulation (Merrill 1984; Weatherford and Gray 1988; Chavas and Emanuel 2010; Chan and Chan 2012), which may reflect the contrasting dynamical regimes between the active convection of the inner core (Didlake and Houze 2013a) and the stratiform precipitation or clear skies of the outer region (Didlake and Houze 2013b). This observation is corroborated in idealized axisymmetric modeling work demonstrating a strong sensitivity to the radial turbulent mixing length of the inner, but not outer, radial wind structure (Rotunno and Bryan 2012; Chavas and Emanuel 2014). These findings suggest that the radial structure of a tropical cyclone may, to leading order, be characterized by the juxtaposition of an inner ascending regime and an outer descending regime, yet deeper quantitative comparisons of these solutions to observations is currently lacking.

More broadly, the terms “size” and “structure” are often used interchangeably in the analysis of tropical cyclones. Indeed, in basic research size is often (though not always) taken to be some metric of the outer circulation (Merrill 1984; Liu and Chan 1999; Knaff and Zehr 2007; Dean et al. 2009; Chavas and Emanuel 2010; Knaff et al. 2014), while in risk analysis size typically refers to the radius of maximum wind due to its relevance to damage potential (Irish et al. 2008; Lin et al. 2012). Perspectives aside, determining which of these metrics is more or less “correct” from a physical standpoint depends principally on their covariability. Ultimately, then, the proper interpretation of any particular length

scale and its variability requires a holistic analysis of the radial wind structure in order to place it within its appropriate dynamical context. Such an analysis necessitates a model for the complete radial wind structure, preferably one that aligns with known tropical cyclone physics and is capable of reproducing its observed characteristics and variability.

Thus, this work seeks insight into the complete radial structure of the tropical cyclone wind field in nature for the dual purposes of testing its theory and improving our understanding of its characteristics (Part I) and variability (Chavas and Lin 2015, manuscript submitted to *J. Atmos. Sci.*, hereafter Part II). Here we first develop a simple new model for the complete tropical cyclone radial wind structure at the boundary layer top by mathematically merging the inner region solution of Emanuel and Rotunno (2011, hereafter ER11) and the outer region solution of Emanuel (2004, hereafter E04). In essence, this is a “first guess” physical model: inner and outer solutions adjoined directly with a vanishingly small radial transition region. Can this simple model reproduce the radial wind structure of real storms in nature? To answer this question, we employ two observational databases of radial wind structure to assess the model and its component parts. First, the outer solution is compared with a QuikSCAT-based global dataset of outer wind structure (1999–2009). Second, the inner solution and, subsequently, the complete model are compared with an HWind-based dataset of radial wind structure in the Atlantic and eastern Pacific basins (2004–12). Section 2 develops the theoretical model. Section 3 describes the observational datasets and methodology for comparing model and data, and the results are presented in sections 4 and 5. Finally, section 6 summarizes key conclusions and explores limitations of this analysis and avenues for future work. Part II will characterize the modes of wind field variability that emerge under an alternative application of this model and their relationship to those found in observations.

2. Theory

a. Review of existing theory

Much of our current theoretical understanding of tropical cyclones is phrased in terms of absolute angular momentum, given by

$$M = rV + \frac{1}{2}fr^2, \quad (1)$$

where r is the radius from the axis of rotation, V is the azimuthal wind, and f is the Coriolis parameter. The low-level circulation of a tropical cyclone can be understood

qualitatively as the partial conservation of absolute angular momentum by inflowing boundary layer air. Beginning at some outer radius r_0 where the rotational wind is zero and absolute angular momentum is a maximum ($M_0 = 1/2 r_0^2 \Omega$), air parcels within the boundary layer flow radially inward toward the center of circulation. In the process, absolute angular momentum is lost as a result of the frictional torque applied to the flow by the surface, while that which remains is gradually converted from planetary to relative angular momentum in the form of the storm circulation. This process continues toward the radius of maximum wind r_m where air parcels ascend in deep convective clouds and flow radially outward aloft near the tropopause.

Quantifying the precise rate at which absolute angular momentum is lost with decreasing radius, though, requires an accounting of the broader dynamics and thermodynamics of the system. Existing theory achieves such a goal, albeit in distinct thermodynamic regimes: the inner ascending region characterized by persistent strong convection (ER11) and the outer descending region characterized by quiescent, convection-free conditions (E04). Here we seek to mathematically merge these two solutions for the purpose of creating a complete solution for the radial distribution of absolute angular momentum, and in turn the radial profile of the rotating wind, in a tropical cyclone. We begin with a review of the theory and solutions for each region.

1) OUTER-REGION STRUCTURE MODEL: E04

In the descending outer region of a tropical cyclone where convection is absent, E04 provides a solution not for the absolute angular momentum itself but for its radial gradient, given by

$$\frac{\partial M_{E04}}{\partial r} = \chi \frac{(rV)^2}{r_0^2 - r^2}, \quad (2)$$

where V is the azimuthal wind in the boundary layer and χ is given by

$$\chi = \frac{2C_d}{W_{cool}}, \quad (3)$$

where C_d is the surface drag coefficient and W_{cool} is the magnitude of the radiative-subsidence rate in the free troposphere. This outer region model assumes convection-free conditions, such that free-tropospheric air subsides at a constant rate W_{cool} under the influence of radiative cooling. Meanwhile, in the boundary layer, surface friction acting on the storm circulation induces a divergent inflow and associated Ekman suction at a rate w_{Ek} through the top of the boundary layer from the free troposphere. From

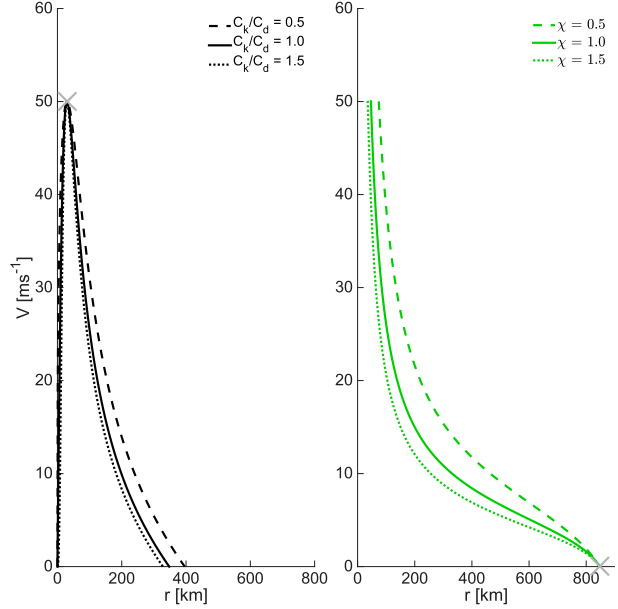


FIG. 1. Example solutions to (left) the inner model [Eq. (6)] with $(r_m, V_m) = (30 \text{ km}, 50 \text{ m s}^{-1})$ and $C_k/C_d = \{0.5, 1, 1.5\}$ and (right) the outer model [Eq. (2)] with $r_0 = 847 \text{ km}$ and $\chi = \{0.5, 1, 1.5\}$. Respective input parameters marked (\times).

mass continuity, the magnitude of w_{Ek} must equal W_{cool} . Thus, Eq. (2) is obtained by combining the definition of w_{Ek} ,

$$w_{Ek} = - \int_0^h \frac{1}{r} \frac{\partial(ru)}{\partial r} \partial z, \quad (4)$$

where $w_{Ek} = -W_{cool}$, u is the radial velocity, and h is the boundary layer depth, with the steady-state slab boundary layer angular momentum budget

$$hu \frac{\partial M}{\partial r} = -C_d |\mathbf{V}| (rV), \quad (5)$$

where the near-surface wind velocity \mathbf{V} is approximated by its azimuthal component V . In short, this model directly connects the thermodynamics of the quiescent free troposphere to the local relative vorticity of the boundary layer flow.

Mathematically, Eq. (2) is a Riccati equation that lacks a known analytical solution but can be solved numerically. Equation (2) has two parameters: χ and r_0 . The former, χ , is a multiplicative factor on the rhs of Eq. (2) and therefore directly modulates the variation of angular momentum (and wind speed) with radius. The latter, r_0 , acts as both a model parameter and the boundary condition for integration. As a result, the radius of any wind speed (e.g., r_{12}) may be used in its place, with r_0 then solved for iteratively using a shooting method, which is significant given that the quantity r_0 is very difficult to

estimate directly in both observations and models (Chavas and Emanuel 2010, 2014). Example solutions are depicted in Fig. 1 (right panel).

As noted earlier, r_0 (or any measure of the outer circulation) is a storm parameter that is observed to vary significantly in nature. In contrast, χ is an environmental parameter that ought to vary relatively slowly across space, as W_{cool} is tied to the free-tropospheric temperature profile, which is dynamically constrained based on weak temperature gradient considerations to remain relatively constant across the tropics for a given climate state (Sobel and Bretherton 2000), while C_d over the open ocean is a function principally of the local wind speed (Donelan et al. 2004) that varies minimally at low wind speeds and otherwise can be taken as the same function from storm to storm. As a result, for practical purposes, r_0 may be regarded as a free parameter; we return to the components of χ in observations in section 3.

2) INNER-REGION STRUCTURE MODEL: ER11

In the ascending inner region of a tropical cyclone, ER11 derives a solution for the radial distribution of angular momentum, given by

$$\left(\frac{M_{\text{ER11}}}{M_m}\right)^{2-(C_k/C_d)} = \frac{2(r/r_m)^2}{2 - (C_k/C_d) + (C_k/C_d)(r/r_m)^2}, \quad (6)$$

where

$$M_m = r_m V_m + \frac{1}{2} f r_m^2 \quad (7)$$

is the angular momentum at the radius of maximum wind¹ and C_k/C_d is the ratio of the exchange coefficients of enthalpy and momentum. Example solutions are depicted in Fig. 1 (left panel).

This inner-region model results from linking the radial distribution of angular momentum at the top of the boundary layer to the stratification of the outflow aloft. Small-scale shear-induced turbulence stratifies the outflow, which translates to an increase in outflow temperature T_0 with radius beyond r_m . Following from classical potential intensity theory, this effect translates to a decrease in the gradient wind with radius at the top of the boundary layer. Note that this model applies

¹ A methodological note: the values of maximum wind and radius of maximum wind are equal to the parameters V_m and r_m in Eq. (6), respectively, in the limit $V_m/f r_m \gg 1$. Thus, we choose parameter values such that the maximum wind and radius of maximum wind in the solution match the desired values.

strictly to the gradient wind; the potential role of supergradient effects is discussed below. Moreover, Eq. (6) does not include the effects of dissipative heating or the pressure dependence of surface enthalpy.

Equation (6) has three parameters: V_m , r_m , and C_k/C_d . The first two are storm parameters that vary significantly in space and time. The third, C_k/C_d , is an environmental parameter that is typically taken to be in the range [0.4, 1] but is the subject of active debate, particularly at high wind speeds in the inner core of a tropical cyclone where effects of sea spray and waves are important (Chen et al. 2013; Bell et al. 2012; Richter and Stern 2014; Potter et al. 2015; Zweers et al. 2015). The solution represents a complete radial wind profile, which is currently used in risk analysis (Lin et al. 2012) and has been demonstrated to perform well in storm surge modeling applications (Lin and Chavas 2012). However, as noted by ER11, the physics are only valid in the ascending region of the storm, thus motivating the development of a structural model that is physically valid in both the ascending and descending regions.

b. Complete radial structure model

We seek to merge the solutions for the inner ascending and outer descending regions given by Eqs. (6) and (2), respectively. Mathematically, this merger imposes the two constraints that M and its radial derivative each be continuous at a merge point, denoted (r_a, V_a) . For the sake of analytical and conceptual insight, we begin with the simplest case of $C_k/C_d = 1$, for which the respective constraints are given by

$$M_m \frac{2}{(r_m/r_a)^2 + 1} = M_a \quad \text{and} \quad (8)$$

$$M_a \frac{2}{r_a [(r_a/r_m)^2 + 1]} = \chi \frac{(r_a V_a)^2}{r_0^2 - r_a^2}, \quad (9)$$

where $M_a = r_a V_a + \frac{1}{2} f r_a^2$ is the angular momentum at the merge point and

$$M_a = M_{\text{E04}}(r_a), \quad (10)$$

which must be solved for by numerical integration of Eq. (2).

This system has three equations [Eqs. (8)–(10)] and seven parameters: six storm-specific unknowns (V_m and r_m in the inner region, r_0 in the outer region, and r_a and V_a at their intersection, and f) and one environmental parameter χ that can be estimated from known environmental conditions. Naturally, we seek to predict the merge point (r_a, V_a) . Thus, given a characteristic value

for χ and a latitude value at the storm center, this leaves two free parameters for external specification from among V_m , r_m , and r_0 .

This construction offers two possible routes. First, the model may take as input r_m and V_m ; conceptually, this approach fixes the inner solution [Eq. (6)] in r - V space and then appends the outer solution [Eq. (2)] to its tail. Second, the model may take either V_m or r_m from the inner region and r_0 from the outer region; conceptually, this approach fixes the outer solution in r - V space and then finds the inner solution that matches. In either case, Eqs. (8) and (9) lead to a quartic function in r_a whose roots can be solved for numerically in conjunction with Eq. (10).

In practice, though, a geometric approach offers useful conceptual insight while achieving the same result. Geometrically, a merge point equates to a tangent point between the two curves. Given the oppositely signed curvatures of the inner and outer solution, the tangent point solution is unique over a wide range of values of all parameters. This fact extends beyond the above case to include deviations of C_k/C_d from unity and radial variations in χ , for which analytical solutions lose their tractability. Thus, for our purposes we obtain the merged solution iteratively by converging toward this geometric constraint, the integration for which is fast [$O(<1)$ s]. An example of a complete model solution is displayed in Fig. 2.

In essence, this is the simplest possible model for the complete radial wind structure that is rooted in existing structural theory—one that assumes an infinitesimal transition between the strongly convecting inner core and the nonconvecting outer region. Note, however, that in the neighborhood of the merge point the two models are mathematically similar by construction. Thus, for the purpose of predicting the radial wind structure, the transition region between strong convection and convection free need not be a single point but rather may be of finite width so long as it is sufficiently narrow.

Next, we test the extent to which this simple model and its component parts can reproduce the radial wind structure of tropical cyclones in nature. For our analysis, we take as input r_m and V_m , as these are by far the most common quantities for analysis in both operational and modeling work. The potential uses of the alternative method taking r_0 as input are discussed in Part II.

3. Observational data and methodology

a. Data

Two databases of radial profiles of the near-surface ($z = 10$ m) azimuthal wind are analyzed:

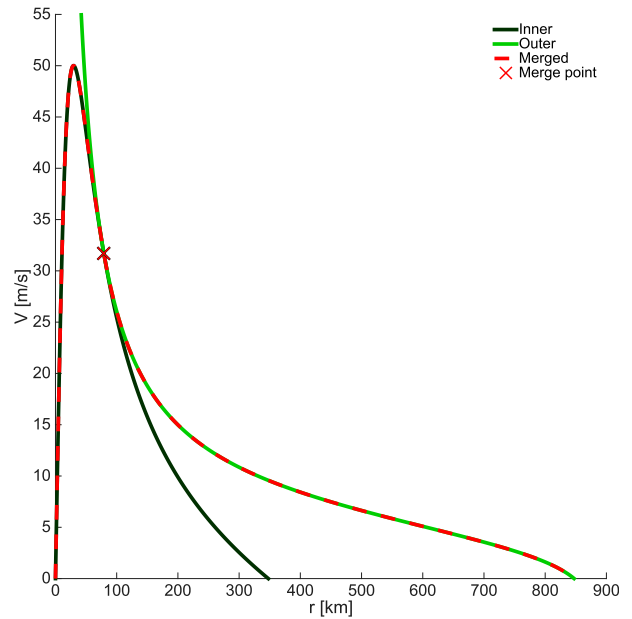


FIG. 2. Complete solution (red dashed) merging the solutions to Eq. (2) with $\chi = 1$ and Eq. (6) with $C_k/C_d = 1$ shown in Fig. 1, taking as input $(r_m, V_m) = (30 \text{ km}, 50 \text{ m s}^{-1})$. The model predicts the outer radius value $r_0 = 847 \text{ km}$. The merge point is $(r_a, V_a) = (79.1 \text{ km}, 31.7 \text{ m s}^{-1})$, which corresponds to $(r_a/r_m, V_a/V_m) = (2.64, 0.63)$.

the QuikSCAT-based QSCAT-R database (Chavas and Vigh 2014) for the outer region (1999–2009, global) and an identically constructed HWind-based dataset (Powell et al. 1998) at small and intermediate radii (2004–12, North Atlantic and eastern Pacific). QuikSCAT and HWind data have approximate horizontal resolutions of 12.5 and 6 km, respectively. For both datasets, an estimate of the background flow is removed for each case prior to calculating the radial profile (see supplementary information). Additionally, QuikSCAT rain-rate data are used to explore the radial structure of convection.

Because of the common occurrence of azimuthally periodic asymmetries (Uhlhorn et al. 2014; Reasor et al. 2000), azimuthal data coverage asymmetry is a principal source of uncertainty in radial profile estimation. To quantify this uncertainty, for each dataset we define a data asymmetry parameter ξ as the magnitude of the vector mean of all gridpoint distance vectors from center as a function of radius. For small $\Delta r/r$, a smaller value of ξ implies lower uncertainty; $\xi = 0$ for data with perfect azimuthal symmetry and $\xi = 1$ in the case of a single data point.

Storm-center latitude and longitude position and local storm translation vector are interpolated from HURDAT and JTWC best-track data. Full details of

all data products are provided in the supplementary information.

b. Methodology: Comparing model and observations

Here we provide an overview of the methodology for comparing the model to observations, whose results are presented in [section 5](#). First, the outer

model given by Eq. (2) is compared with the QuikSCAT database. For the purposes of comparing with real-world observations, we constrain C_d to be a piecewise constant–linear–constant function of V whose parameters are optimally estimated directly from the data of [Donelan et al. \(2004\)](#). This function is given by

$$C_d = \begin{cases} 6.16 \times 10^{-4} & V \leq 6 \text{ m s}^{-1} \\ 5.91 \times 10^{-5} \times V + 2.614 \times 10^{-4} & 6 \leq V \leq 35.4 \text{ m s}^{-1} \\ 2.4 \times 10^{-3} & 35.4 \text{ m s}^{-1} \leq V \end{cases} \quad (11)$$

Unlike C_d , we currently lack an observational specification for W_{cool} . Thus, W_{cool} replaces χ as the environmental free parameter in the outer wind model. Here we take W_{cool} to be constant and seek to optimally estimate its value from the model fit to the QuikSCAT data. The Coriolis parameter f is taken as its value at the latitude of the storm center. We note that the qualitative behavior of the model solution presented in the previous section is not sensitive to the choice of constant or variable C_d in the outer region.

Second, the inner model given by Eq. (6) is compared with the HWind database, where we retain only profiles whose peak azimuthal-mean wind speed exceeds 15 m s^{-1} to remove very weak cases. As noted above, the value of the environmental free parameter C_k/C_d is the subject of active debate. Thus, its value is first optimally estimated from the model fit to the HWind data.

Finally, given optimal estimates of W_{cool} for the outer region and C_k/C_d for the inner region, the complete model is compared with the HWind database, again taking V_m and r_m as input parameters, and contrast the results to that of the inner model alone.

Note that these datasets are valid near the surface, whereas ideally one would test the model against observations at the top of the boundary layer. However, datasets of comparable quality or quantity at the gradient level are not currently available. Moreover, the nature of the hurricane boundary layer and its role in mediating wind speeds from gradient level to the surface, including the effects of gradient wind imbalance, are not easily accounted for² and remain a subject of active research ([Powell et al. 2003](#); [Kepert 2010](#); [Gopalakrishnan et al. 2013](#); [Kepert 2013](#); [Sanger et al. 2014](#)). As a result, here we do not explicitly account for the boundary layer, instead exploring the extent to

which a model theoretically valid at the boundary layer top can reproduce near-surface wind structure; further discussion is provided in [section 6](#).

4. Radial structure in observations

We begin simply with an exploration of the characteristic radial wind structure in a tropical cyclone from our observational databases. [Figure 3](#) displays a subset of cases from the North Atlantic basin for which HWind and QuikSCAT data are available nearly concurrently. These cases ($N = 31$) meet the following criteria: (i) time difference between HWind and QuikSCAT of less than 2 h, (ii) peak HWind radial profile wind speed V_m exceeding 25 m s^{-1} , and (iii) difference in wind speed at the transition point less than 3 m s^{-1} .

From this subset emerges a common overall structure: significant variability in the inner core (r_m and V_m span a range of $[12.3, 111.2] \text{ km}$ and $[25.1, 57.6] \text{ m s}^{-1}$, respectively), rapid decay of wind speed with radius immediately beyond r_m , and a long tail at larger radii where wind speed decays increasingly gradually with radius. Additionally, the length scale of the outer circulation varies significantly: for example, the radius of 12 m s^{-1} spans a range of $[142, 468] \text{ km}$. This characteristic structure qualitatively resembles our complete model solution shown in [Fig. 2](#).

5. Model versus observations

We now quantify the model fit to observations. We start with a simple demonstration example for a storm snapshot. Subsequently, we perform a comprehensive comparison of each model component and the complete model with the observational databases, including optimal estimation of the environmental parameters and discussion of relationships of the estimated values to their underlying physics.

²Typically wind speeds are simply reduced from gradient level by a factor of 0.85 – 0.9 ([Powell et al. 2003](#)).

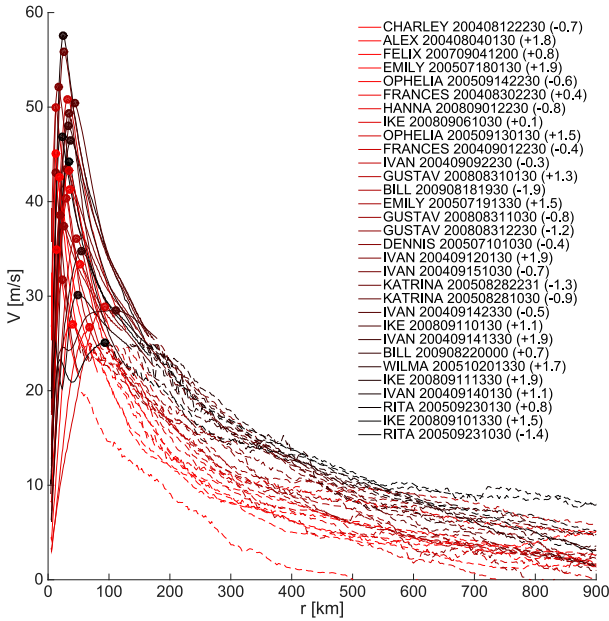


FIG. 3. Subset of radial profiles of the azimuthal wind from combined HWind and QuikSCAT observations; dots denote (r_m, V_m) . Curves colored from red to black in order of increasing r_{12} . Legend lists storm name, HWind date and time (YYYYMMDDHHMM), and time difference (h) between HWind and QuikSCAT data. HWind data shown for $r \leq \max(r_{25}, 50 \text{ km})$ and QuikSCAT data shown elsewhere. Subset includes cases with valid HWind and QuikSCAT data less than 2 h apart, $V_m \geq 25 \text{ m s}^{-1}$, and $\Delta V \leq 3 \text{ m s}^{-1}$ between HWind and QuikSCAT data at r_{25} ($N = 31$).

a. Example: Ivan on 14 September 2004

Figure 4 displays the fit of the inner model alone as well as the complete model to data for Hurricane Ivan on 14 September 2004, when both HWind (1330 UTC) and QuikSCAT (1134 UTC) data are available at comparable times with highly symmetric data coverage out to large radii ($\xi \leq 0.5$ for $r \leq 800 \text{ km}$). QuikSCAT data are used in the outer region radially outward of the radius of 25 m s^{-1} and HWind data are used radially inward. The inner and complete models are fit to HWind $(r_m, V_m) = (32.7 \text{ km}, 48.0 \text{ m s}^{-1})$, where we set $C_k/C_d = 0.8$ and $W_{\text{cool}} = 2.5 \text{ mm s}^{-1}$, both of which are plausible values based on past research (detailed parameter estimation and discussion is provided below). The merge point between the inner and outer region models is located at $(r_a, V_a) = (73.9 \text{ km}, 35.9 \text{ m s}^{-1})$.

First and foremost, the complete model significantly improves upon the inner model alone in its representation of the wind structure beyond the inner core. Indeed, as components of the complete model, both the inner and outer models are largely capable of reproducing their respective regions. In the vicinity of the radius of maximum wind, the inner model reproduces the local radial wind structure for given (r_m, V_m) and the chosen

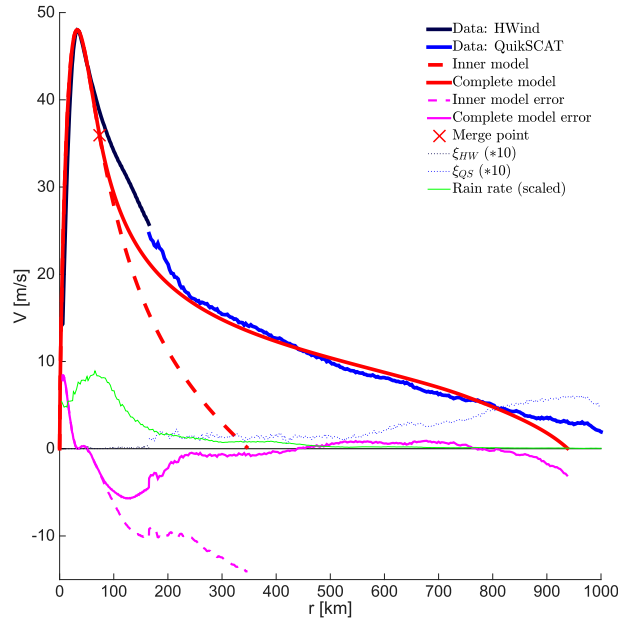


FIG. 4. Example of model fit to data for Hurricane Ivan at 1330 UTC 14 Sep 2004. Data from HWind (black) and QuikSCAT (blue; 1134 UTC), with fit of inner model alone (red dashed) and complete model (red solid) and respective model errors (pink) for $(r_m, V_m) = (32.7 \text{ km}, 48.0 \text{ m s}^{-1})$, $C_k/C_d = 0.8$, and $W_{\text{cool}} = 2.5 \text{ mm s}^{-1}$. Respective data asymmetry parameters ξ (dotted; rescaled by factor of 10) displayed as a function of radius, as well as radial structure of QuikSCAT-estimated precipitation rate (green; scaled).

value of C_k/C_d . Perhaps more surprisingly, in the broad outer region, the outer model reproduces the observed winds with absolute errors of less than 1 m s^{-1} over the wide annulus spanning $r \in [250, 850] \text{ km}$. For $r > 850 \text{ km}$, the model approaches zero more rapidly than observed, though data coverage asymmetry becomes large at such large radii, indicating greater uncertainty. The dominant region of misfit lies just beyond the merge point ($r \in [75, 175] \text{ km}$, corresponding to $r/r_m \in [2.3, 5.4]$). At these intermediate radii, the model underestimates the observed wind speeds, with a maximum (negative) error (model-data) of 5.4 m s^{-1} at $r = 130.5 \text{ km}$. Notably, in this region the descending outer model is applied, yet the rain-rate data shown in Fig. 4 indicate that at least some intermittent convection is likely occurring. Nevertheless, the model is capable of capturing the overall qualitative radial structure as well as the quantitative structure at both small and large radii.

b. Outer model

The outer wind model of Eq. (2) is physically valid for the region beyond the storm inner core where convection is absent. Approaching very large radii, however, it

is increasingly likely that QuikSCAT data coverage becomes highly asymmetric (the maximum possible cross-swath radius of perfectly symmetric data is 900 km) and the assumption of constant background flow loses its validity. Furthermore, the large variability in storm size implies that fixed radial bounds cannot be used to define the outer region across storms. With these issues in mind, we take a simple approach based instead on V , which has a monotonic, one-to-one relationship with r beyond r_m , and define our test region as the annulus of radii of wind speeds in the range $V \in [5, 20] \text{ m s}^{-1}$ beyond r_m . Note from Fig. 3 that this wind speed range corresponds to a wide range of annuli, from [54, 280] km in the case of Charley at 2230 UTC 12 August 2004 to [148, 1131] km in the case of Gustav at 1300 UTC 31 August 2008. Finally, to filter out cases with poor data coverage we utilize the data asymmetry parameter, imposing the requirement of $\xi_{QS} \leq 0.5 \text{ km}$ at all radii within this test region ($N = 470$).

A model solution requires a single point (integration constant) and a value of W_{cool} . Thus, for each case, we fit the outer wind model to the observed r_{12} and then seek the value of W_{cool} in the range $[0.2, 20] \text{ mm s}^{-1}$ for each storm that minimizes the total least squares error (LSE) summed over all radii within the test region. The length scale r_{12} has been used in past work as an ideal wind radius that balances high measurement accuracy, sufficient data coverage, and minimal noise from both moist convection and variations in the environmental flow (Chavas and Emanuel 2010). The distribution of best-fit W_{cool} is displayed in Fig. 5, where data have been binned by Saffir–Simpson category of the best track intensity V_m^{BT} . Data are plotted on a log scale, as W_{cool} is a multiplicative parameter in Eq. (2) and thus multiplicative rather than additive changes govern the parameter’s influence. The distributions are qualitatively lognormal with a median value of approximately 2 mm s^{-1} that remains nearly constant across intensity bins ($[1.6, 2.0] \text{ mm s}^{-1}$).

For comparison, a simple calculation provides a theoretical prediction of W_{cool} . Radiative-subsidence balance dictates that radiative cooling is balanced by subsidence warming in a stably stratified atmosphere,

$$Q_{\text{cool}} = W_{\text{cool}} \frac{\partial \theta}{\partial z}, \quad (12)$$

where Q_{cool} is the radiative cooling rate (of the potential temperature), θ is potential temperature, and z is altitude. For an atmosphere corresponding to a parcel lifted along a reversible moist adiabat from the sea surface of temperature of 302 K, corresponding to a typical tropical warm pool temperature, with 80% boundary layer relative humidity and a characteristic atmospheric

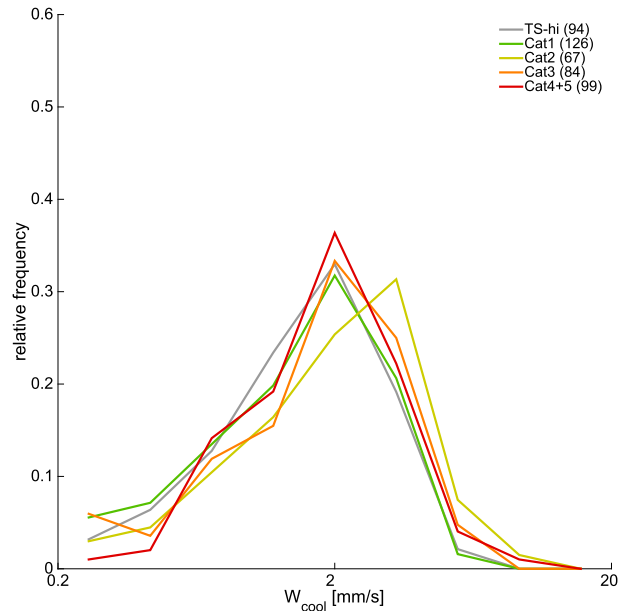


FIG. 5. Probability distributions of the optimal value of W_{cool} in outer wind model, with corresponding median values denoted by \times along x axis. Distributions are disaggregated by Saffir–Simpson category of best-track intensity V_m^{BT} (sample size in parentheses); “TS-hi” corresponds to tropical storms with $V_m^{\text{BT}} \geq 25 \text{ m s}^{-1}$. Optimization is based on minimizing least squares error between model and observations over radii of wind speeds in range $V \in [5, 20] \text{ m s}^{-1}$, with model fit to the observed r_{12} .

radiative cooling rate of 1 K day^{-1} , Eq. (12) gives a value of $W_{\text{cool}} = 1.9 \text{ mm s}^{-1}$, nearly uniform with altitude below $z = 10 \text{ km}$. This prediction is very close to the median value estimated from our model fit. This value is also very close to that found in the simulation of Davis (2015). We note that this value is significantly smaller than that used in Chavas and Emanuel (2010), indicative of the long tail in the wind profile at radii approaching r_0 evident in Fig. 3.

Using the optimized values of W_{cool} , the performance of the outer model is displayed in Fig. 6. Model error is defined as the difference between the model and data for each individual case, where the model is fit to r_{12} and W_{cool} is optimized for each storm as above; error percentiles are then calculated across all included cases as a function of radius. Absolute values of median model error are less than 0.5 m s^{-1} at all radii of wind speeds less than r_{12} (where error is zero by definition). The model shows a slight but increasing negative bias approaching r_{20} , with (negative) error maximized at approximately -1.5 m s^{-1} at r_{20} . Error distributions across intensity bins are very similar at all radii, particularly for radii beyond r_{12} . Additionally, the width of the test region ($V \in [5, 20] \text{ m s}^{-1}$) is nearly constant with intensity, with median values by intensity bin spanning the narrow range [556, 594] km

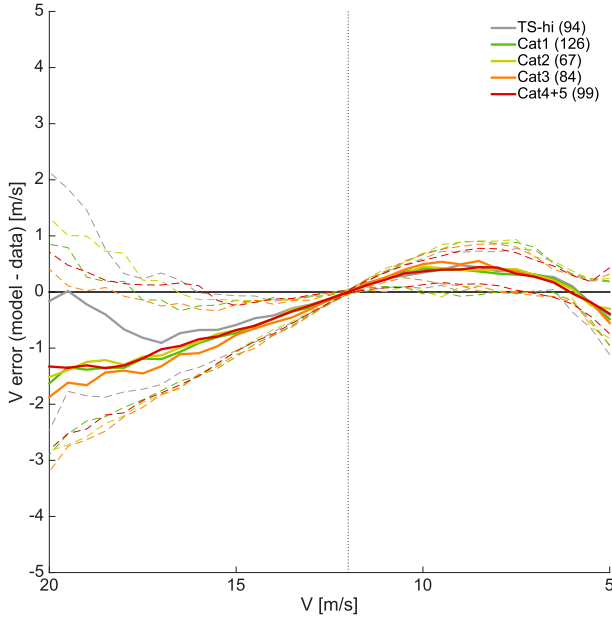


FIG. 6. Profiles of median model error in V (model–QuikSCAT obs) for the outer model as a function of wind speed over test range $V \in [5, 20] \text{ m s}^{-1}$, where W_{cool} is taken as its optimized value whose distributions are shown in Fig. 5. Dashed lines denote interquartile range. Data are binned by V_m^{BT} as in Fig. 5 (sample sizes in parentheses). The median width of the test annulus is 582 km.

(median value of 582 km for all cases). This invariance in both error profile and median estimate of W_{cool} with intensity (Fig. 5) is an indication of the aforementioned insensitivity of the outer region wind field to inner-core variability found in observations and models.

In combination, Figs. 5 and 6 indicate that the simple outer wind model given by Eq. (2) appears to successfully capture the fundamental physics of the radial structure of the broad outer descending region in tropical cyclones in nature. The intrabin variance of W_{cool} likely represents the combination of observational error due to variability in data coverage and real transient variability in outer storm structure. In particular, although weak temperature gradient considerations strongly limit horizontal variations in tropical lapse rates (Sobel and Bretherton 2000) and therefore W_{cool} [cf. Eq. (12)], this quantity likely still varies slowly across space and with the seasonal cycle owing to local variations in sea surface temperature. Furthermore, W_{cool} depends on the radiative cooling rate, which is sensitive to both column water vapor and cloud water path, quantities that may vary both at large scales as well as with radius within a given storm. Indeed, recent work has demonstrated that water–radiation feedbacks can have significant impacts on storm structure and evolution (Bu et al. 2014; Didlake and Houze 2013b), including the effects of high-altitude cirrus clouds that are common to the outflow layers of tropical cyclones and

often extend radially outward beyond the convecting inner core (Molinari and Vollaro 2014). Finally, there are potential dependencies of the background climate state itself on the prevalence of tropical cyclones, which are known to cause a drying of the large-scale environment (Tobin et al. 2012) akin to the effect of convective aggregation in general in radiative–convective equilibrium (Wing and Emanuel 2014). The magnitude of such climate-scale effects on the space–time variability of W_{cool} is unknown though may be small relative to that induced by synoptic and subseasonal variability of environmental water vapor.

c. Inner model

The inner wind model of Eq. (6) represents a solution for the complete radial wind profile, but its underlying physics are valid only in the ascending inner core. Given a value for C_k/C_d , Eq. (6) requires as input parameters V_m and r_m , which are taken directly from the HWind radial profile.

First, though, we seek the optimal estimate of C_k/C_d in the inner region from the data. To compare directly with Eq. (6), we calculate M/M_m as a function of r/r_m for the set of cases for which $V_m/f r_m \geq 10$ to align with the underlying assumptions of the model itself as detailed in ER11; this assumption is valid for the majority of cases above hurricane intensity. Because the region beyond r_m in which the model is expected to be valid is relatively narrow, fitting the parameter to each individual case is too noisy to generate a meaningful distribution of individual cases akin to that for W_{cool} in Fig. 5. Instead, optimization is performed by calculating the median profile of M/M_m within prescribed intensity bins and then determining the LSE-minimizing value of C_k/C_d for the median profile within the annulus of normalized radii given by $r/r_m \in [1, 2.5]$. As with the QuikSCAT database, to filter out cases with poor data coverage we impose the requirement $\xi_{\text{HW}} \leq 0.5$ at all radii within this test region ($N = 603$).

The result is displayed in Fig. 7, which shows the variation of C_k/C_d with azimuthal-mean peak intensity in bins of width 5 m s^{-1} . At lower intensities, with $V_m < 40 \text{ m s}^{-1}$, the values of C_k/C_d lie in the range $[0.4, 0.6]$, consistent with existing estimates (Chen et al. 2013; Bell et al. 2012). However, the optimal estimate increases monotonically with intensity, particularly for the highest intensities where the validity of the model assumptions is most likely to be robust. The optimal estimate for the highest intensity bin is approximately 1. Results are not sensitive to the threshold of $V_m/f r_m$, with only a slight decrease in the estimate at low intensity when this constraint is removed. Moreover, Eq. (6) exhibits a slightly more rapid decrease of M/M_m with

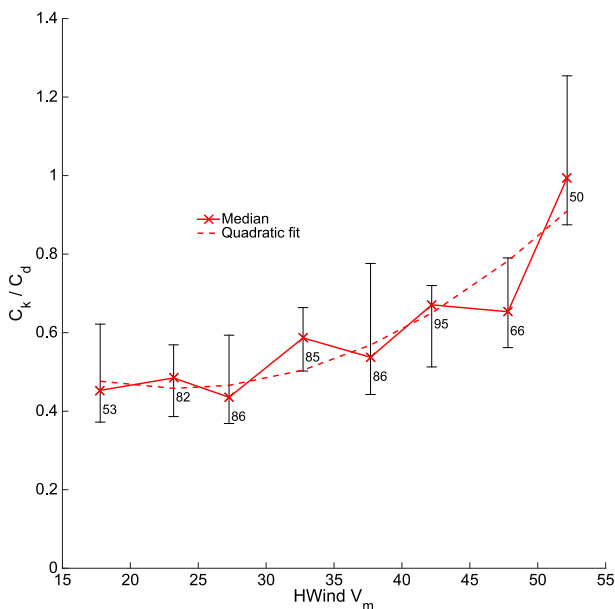


FIG. 7. Best-fit C_k/C_d in Eq. (6) to HWind data as a function of peak azimuthal-mean wind speed V_m binned at intervals of 5 m s^{-1} ; final bin includes all cases above 50 m s^{-1} . Crosses are values estimated from fit of model to median profile of M/M_m as a function of r/r_m within each bin for cases where $V_m/r_m \geq 10$. Bars indicate 95% confidence interval of the median, calculated from 100-member bootstrap resampling of median profile of M/M_m . Simple quadratic fit to median data shown (dashed) is given by $C_k/C_d = 0.00055V_m^2 - 0.0259V_m + 0.763$. Bin sizes denoted below each data point.

normalized radius than that found in observations, and as a result the absolute value of C_k/C_d is sensitive to the upper bound in normalized radius imposed for the optimization; the value of C_k/C_d decreases when a larger radial range is used. However, the relative values and overall trend are not sensitive to the upper bound.

The upward trend of C_k/C_d with intensity appears to disagree with aforementioned observational estimates, which typically predict a constant or even slightly decreasing trend, albeit with large error bars at high wind speeds. However, this result may suggest a shift in the nature of air–sea fluxes of enthalpy and momentum at such high wind speeds, perhaps implicating an outsized role of sea spray in enthalpy fluxes (e.g., Richter and Stern 2014; Zweers et al. 2015). Alternatively, it may indicate that the myriad complexities of real-world storms not accounted for by the simple theoretical model, taken in combination, impose a nonnegligible modification to the gradient wind solution. These complexities include boundary layer effects such as supergradient winds, radial variation of C_k/C_d , the spatial structure of mixing-induced cooling of the sea surface temperature field, and the inclusion of dissipative heating and the pressure dependence of saturation enthalpy.

In particular, the existence of supergradient wind speeds near the radius of maximum wind in the boundary layer (Bryan and Rotunno 2009; Smith and Montgomery 2008), an effect whose magnitude is expected to increase with intensity (Stern and Nolan 2011; Stern et al. 2014), would locally enhance wind speeds just beyond r_m ; the result would be a steeper radial gradient in wind speed, which equates to an effective enhancement of the parameter C_k/C_d in Eq. (6). Similarly, dissipative heating acts in the same direction as increasing C_k ; its inclusion in a numerical integration of the full model presented in ER11 reduces the best-fit value of C_k/C_d in the highest intensity bin in Fig. 7 by 15%. On the other hand, inclusion of the pressure dependence of saturation enthalpy in the numerical integration alters the model behavior in more complex ways, including inducing nonmonotonicity in the structural dependence on C_k/C_d . Ultimately, the independent, quantitative effects of each of these factors cannot be extricated from the data and instead require further investigation in an idealized experimental setting.

Finally, the mismatch may indicate a flaw in the underlying physics of the model, given that the optimized values of C_k/C_d that differ most strongly with existing estimates occur at those high intensities at which the model is expected to perform best. Indeed, as storm intensity increases, convection is known to become more intense, more axisymmetric, and more confined to the vicinity of the radius of maximum winds (Dvorak 1984), all of which should enhance the likelihood of the onset of turbulence in the outflow layer. Furthermore, strong signatures of Kelvin–Helmholtz turbulence have been found in the outflow layer of tropical cyclones, particularly at higher intensities (Molinari et al. 2014). However, the underlying physical assumptions of the model in the context of a fully three-dimensional storm in nature are not rigorously tested here, but this is undoubtedly a worthy endeavor.

Ultimately, for our purposes, we choose to treat C_k/C_d simply as a tunable environmental parameter whose best-fit values appear plausible as input to a model capable of capturing the characteristic wind profile near r_m . Our results are insufficient to conclusively establish the validity of the underlying physics of the model or the role of the aforementioned extenuating effects on modifying the theoretical solution in real-world storms. Note that these results may explain why this model with $C_k/C_d = 1$ has been found to perform well in storm surge and wind risk simulations (e.g., Lin and Chavas 2012; Lin et al. 2012), which are primarily sensitive to the highest-intensity storms.

Returning to the radial wind structure, Fig. 8 displays the statistics of model error as a function of normalized

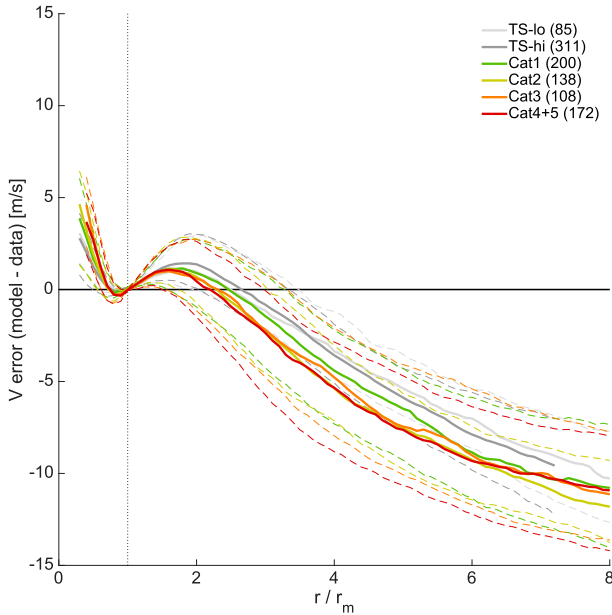


FIG. 8. Profiles of median model error in V for the inner model (model minus HWind obs) as a function of r/r_m . Error statistics calculated from direct fit of model to observed wind profile for each individual case, with C_k/C_d value calculated using quadratic fit equation of Fig. 7. Dashed lines denote interquartile range. Data shown for all radii with valid error data for at least 80% of sample size. Intensity binning as in Fig. 6 (sample sizes in parentheses), with “TS-lo” corresponding to storms with $V_m^{BT} < 25 \text{ m s}^{-1}$. Small adjustment applied within the eye as described in the text.

radius, binned by intensity, where C_k/C_d is taken to follow the quadratic fit to the data shown in Fig. 7 given by $C_k/C_d = 0.00055V_m^2 - 0.0259V_m + 0.763$. Error statistics are calculated for the comparison of the model to the full dataset without constraint on V_m/r_m so as to provide an assessment of model performance across all available cases ($N = 1014$). Within the eye, the inner model is not formally valid and tends to overestimate the winds; thus, we apply a small adjustment in this region by reducing the solution given by Eq. (6) for $r/r_m < 1$ by a factor $(r/r_m)^\alpha$, where $\alpha = 0.15$ minimizes model bias in the range $r/r_m = [0.75, 1]$ across all intensities.³ As such, the inner model performs well for $r/r_m \leq 2.5$, with errors typically less than 2 m s^{-1} . Meanwhile, at larger radii, the model increasingly underestimates the observed wind

³ The eye is often modeled using a linear or slightly superlinear profile of V/V_m as a function of r/r_m , under the assumption that eddies restore the eye toward a state of solid-body rotation (Smith 1980; Emanuel 1995). Notably, for $C_k/C_d = 1$, the asymptotic solution of Eq. (6) for $r/r_m \rightarrow 0$ is linear with r/r_m . However, the linear model substantially underestimates the observed wind profiles in the eye, particularly just inside of r_m . Thus, the modification of the eye applied here corresponds to a slightly superlinear wind profile at small radii in accordance with eddy-restorative eye theory.

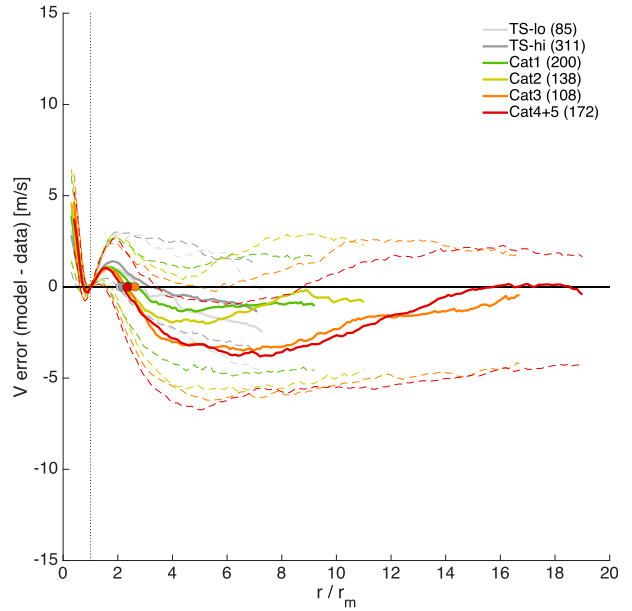


FIG. 9. As in Fig. 8, but for the complete model out to larger normalized radii, with W_{cool} fixed at its climatological value of 2 mm s^{-1} . Circles denote median merge point r_d/r_m .

field, with (negative) errors of approximately 5 m s^{-1} at $r/r_m = 4$ and higher values beyond; this result is similar across all intensity bins. This is not surprising, as the inner model is not expected to properly represent the outer descending region of the storm.

d. Complete model

We now test our complete model merging Eqs. (6) and (2), where the same inputs (r_m, V_m) and parameter C_k/C_d are used as for the inner model case of Fig. 8, and we fix W_{cool} at the approximate climatological value of 2 mm s^{-1} found in Fig. 5. Figure 9 displays the error profile binned by best-track intensity. The model now does an admirable job at all normalized radii and across all intensity bins, providing a substantial reduction in model error beyond $r/r_m = 3$ compared to the inner model alone. For intensities at and above category 1, model underestimation reaches a maximum in the range of $2\text{--}5 \text{ m s}^{-1}$ in the vicinity of $r/r_m = 6$, beyond which error tends to gradually decrease out to very large radii; for categories 3–5, median model error approaches zero at approximately $r/r_m = 14$. The model performs surprisingly well at low intensity, too, despite the fact that the model assumptions are increasingly unlikely to be valid for such cases. The model error profiles are quantitatively similar to the case study example of Fig. 4.

The relative constancy of model error with radius at large normalized radii in Fig. 9 mirrors the good fit of the outer model to the QuikSCAT observations shown in

Fig. 6. However, there remains an overall negative bias in the much of the outer region of the storm across all intensity bins. Despite the good performance of the inner and outer models within their respective regions of validity (Figs. 6 and 8), the existence of a negative bias in the merged model indicates that this model is not quite sufficient to capture the structure of the storm at all radii simultaneously. Indeed, merging the two models eliminates the constraint that the outer model be fixed to an observed wind radius in the outer region (r_{12} in Figs. 5 and 6) and instead ties the radial position of the outer wind model directly to the inner-core structure. Thus, the negative bias in V , which is equivalently a negative bias in r , is evidence for the existence of a transition region of nonnegligible width between the strongly convecting inner region and nonconvecting outer region not captured with this model. Notably, this bias decreases with intensity in the far outer region, again consistent with expectations that the model assumptions are most valid at high intensity when the storm is more axisymmetric and convection is more sharply confined to the vicinity of r_m .

For the purpose of demonstration, Fig. 10 displays the observed median radial structure and model fit within each intensity bin. The observed profiles are calculated by first taking the median profile of M/M_m as a function of r/r_m and subsequently converting the result to V using median parameter values of V_m , r_m , and f within each intensity bin. Meanwhile, the corresponding model profiles are taken as the solution using the same median parameter values for each bin. The salient features of the error profiles of Fig. 9 are evident, including both the underestimation at intermediate radii and the improved model performance over the inner model at large radii, especially at high intensities.

To further probe the radial extent of convection, Fig. 11 displays the characteristic radial structure of QuikSCAT-estimated precipitation rate P and corresponding merge point radius r_a for the subset of cases with sufficient HWind and QuikSCAT rain-rate data in the inner core, such that rain-rate and (r_m, V_m) data are available simultaneously. These cases ($N = 24$) meet the following criteria: (i) time difference between HWind and QuikSCAT of less than 2 h, (iii) HWind $V_m \geq 20 \text{ m s}^{-1}$, and (iii) $\xi \leq 0.5$ for $r \leq r_a$ for both datasets. Figure 11 also shows the distribution of P_a/P_{\max} , where $P_a = P(r = r_a)$, which indicates that r_a is typically located at or near the outer edge of the strongly convecting inner core. Although convection diminishes steadily with normalized radius, the data demonstrate that at least intermittent convection, perhaps in the form of spiral rainbands, often extends well beyond r_a . This is an indication that the complete model incorrectly

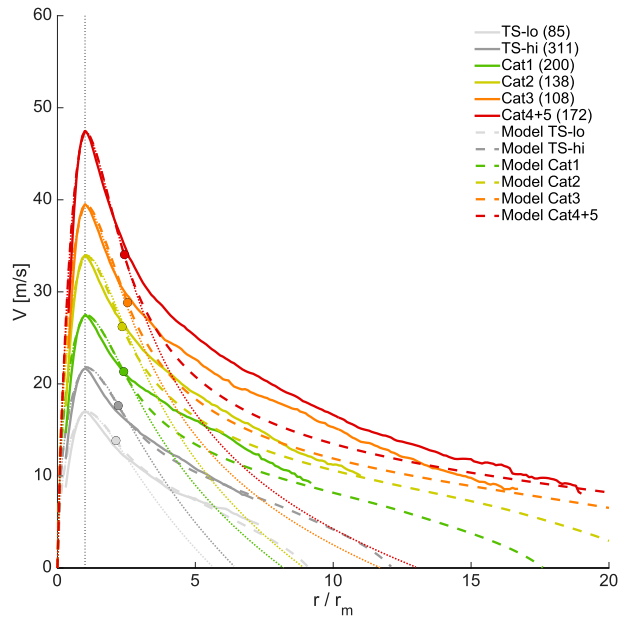


FIG. 10. Characteristic radial profiles from HWind observations (thick solid) and complete model fit (thick dashed) with merge point (circle) for set of cases presented in Fig. 9; fit to inner model alone also shown (dotted) for comparison. Observed profiles calculated from median profile of M/M_m as a function of r/r_m , then converted to V using median parameter values of V_m , r_m , and f within each intensity bin; data shown for all radii with valid wind speed data for at least 80% of sample size. Each model profile calculated as solution for given set of median parameter values (from low to high intensity: $V_m = 17.0, 21.7, 27.5, 34.0, 39.5, 47.5 \text{ m s}^{-1}$, $r_m = 60.1, 53.9, 38.8, 38.3, 24.2, 23.8 \text{ km}$, and $f = 5.5, 6.1, 6.0, 6.1, 5.6, 5.1 \times 10^{-5} \text{ s}^{-1}$), with C_k/C_d estimated from best-fit curve of Fig. 7 and $W_{\text{cool}} = 2 \text{ mm s}^{-1}$.

assumes a quiescent atmosphere at intermediate radii where some convection is typically still occurring. Indeed, the forcing of convection at intermediate radii has been shown to enhance the inward flux of boundary layer angular momentum from larger radii and thus accelerate the tangential winds locally (Chan and Chan 2013; Xu and Wang 2010). This effect would result in wind speeds exceeding that which would be expected in a fully quiescent environment, as is borne out in the data. We note that one might be tempted to interpret this region of intermediate convection to be some blend of the ascending inner and descending outer models. However, beyond the merge point, the inner ascending model in fact performs worse than the outer descending model (Fig. 10), and thus a smoothed version of the two models cannot eliminate the corresponding low bias; instead, a distinct model for intermittent convection is required.

Overall, the complete model appears capable of credibly capturing much of the characteristic radial structure of a tropical cyclone, particularly at higher

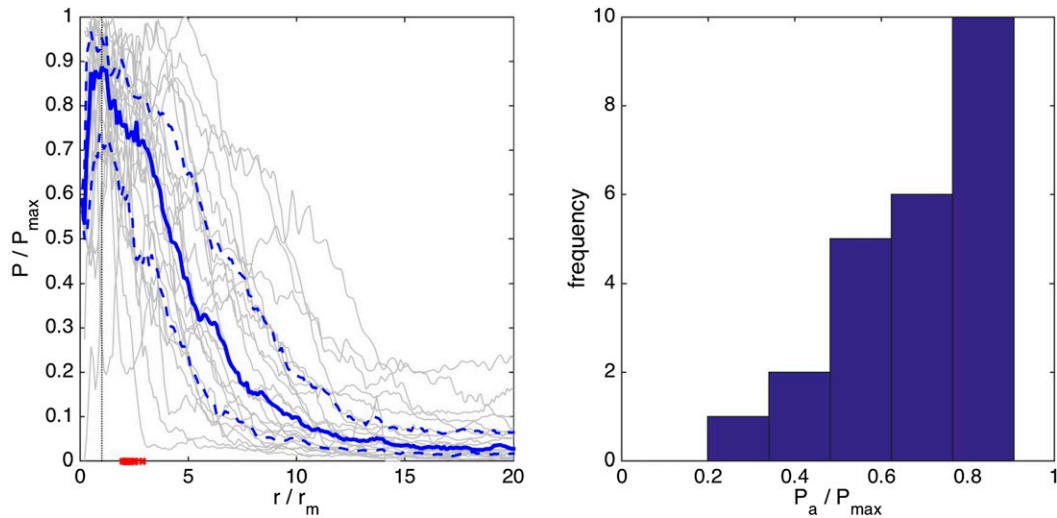


FIG. 11. Relationship between radial structure of precipitation and model merge point r_a . (left) Median (solid blue) radial profile of QuikSCAT-estimated precipitation rate normalized by its maximum value P_{\max} as a function of normalized radius, with interquartile range (dashed blue) and all data (gray) and corresponding values of r_a (red \times symbols) from fit of complete model to HWind (r_m, V_m) with $W_{\text{cool}} = 2 \text{ mm s}^{-1}$. (right) Histogram of $P_a = P(r = r_a)$ normalized by P_{\max} . Subset ($N = 24$) includes cases with valid HWind and QuikSCAT data less than 2 h apart, $V_m \geq 20 \text{ m s}^{-1}$, and $\xi \leq 0.5$ at all radii $r \leq r_a$ for both HWind and QuikSCAT.

intensity consistent with its underlying assumptions. The model also performs surprisingly well at low intensity despite the broader and more disorganized field of convection characteristically associated with weaker systems, seemingly at odds with the assumptions and approximations of our model that are expected to break down in such conditions. As a result, we view this latter result as largely fortuitous, though nonetheless beneficial for practical applications.

6. Summary and conclusions

We have mathematically merged existing theoretical solutions in the inner ascending region characterized by persistent strong convection (ER11) and the outer descending region where convection is absent (E04) to create a model for the complete radial wind structure of the tropical cyclone wind field at the top of the boundary layer. The outer solution is found to reproduce the observed outer wind field of the storm within the broad annulus bounded by wind radii r_{20} and r_5 , with a median absolute error of less than 1 m s^{-1} at most radii except for slightly larger underestimation near r_{20} . This result provides strong evidence that the outer solution is accurately capturing the fundamental physics of the descending outer region of the storm in nature. The inner solution is found capable of reproducing the inner-core structure inward of $2.5r_m$, though its predicted values of C_k/C_d appear to disagree with existing estimates at high intensity. The solution increasingly underestimates the

wind field at larger radii where convection diminishes and the underlying model assumptions are expected to breakdown. The merged model largely, though not entirely, eliminates this underestimation. A residual negative bias exists at all radii beyond the inner core, maximized at approximately $6r_m$, though it approaches zero at large radii for high-intensity storms (categories 3–5). This underestimation at intermediate radii is interpreted as the need for a transition model of intermittent or shallow convection between the inner and outer region models, though it may alternatively reflect a radial dependence of the radiative-subsidence rate within a given storm due to the effects of high clouds or water vapor on radiative cooling.

Overall, despite its simplicity, the model appears to credibly capture the characteristic radial structure of the tropical cyclone wind field in nature and in a manner consistent with existing, distinct theories for the ascending and descending thermodynamic regimes. Though the direct merger of the inner ascending and outer descending solutions is a product of mathematical convenience, this work indicates that the physical world is not far off for reasonably intense storms, suggesting that the model may represent the attractor state toward which storm structure evolves in conjunction with the analytical solution for the attractor of storm intensity derived in Tang and Emanuel (2010).

Though these apparent successes are encouraging, the model and its evaluation are also subject to limitation. First and foremost, the analysis neglects the role of the

boundary layer as an intermediary between the gradient level and the surface. Our results suggest that its effect on the characteristic radial wind structure outside of the inner core may be relatively small on average, though we cannot rule out its significance. In the inner core, though, the mismatch between the predicted value of C_k/C_d and existing estimates at high intensity is likely tied to the combination of uncertainties in our understanding of surface exchange processes; a lack of accounting of a variety of key real-world effects associated with the boundary layer (Abarca and Montgomery 2014; Kepert 2013), most notably supergradient winds, and ocean interaction; and/or flaws in the underlying physics of the model itself. Quantitative testing of the contributions of each of these hypotheses in an idealized, three-dimensional setting is needed for conclusive attribution of the mismatch between model and observations. Second, the merge point between the two models consistently lies within the region of active convection and, as such, the physics of the model is formally wrong at intermediate radii beyond the merge point regardless of whether the model correctly reproduces the wind field there. Given that this model directly superposes ascending and descending regimes, one hypothesis for a transition region of finite width is zero net vertical motion corresponding to radiative–convective equilibrium. Third, this model applies specifically to the azimuthal-mean flow, yet asymmetries abound in real-world storms whose effects are not studied here; comparative analysis of a smaller subset of annular storms, which exhibit a high degree of azimuthal symmetry and minimal convection beyond the inner core (Knaff et al. 2003), against those cases with strong asymmetries may reveal additional insights for understanding and modeling the full two-dimensional flow field. Finally, though we employ a simple data coverage asymmetry parameter in an effort to minimize potential biases imposed by imperfect spatial data coverage, a better approach would quantitatively account for the uncertainties imposed by asymmetric data coverage when testing the model against observed radial profiles, such that all profiles could be used and their variable uncertainties (both within profiles as a function of radius and across profiles) would be incorporated into the final results; such an approach is not straightforward but is undoubtedly a worthy endeavor.

Nonetheless, for practical purposes the model offers a simple theoretical basis of comparison for future observational and modeling studies of tropical cyclone size and structure. Furthermore, this work offers the potential to place individual wind radii within a holistic, physics-based structural framework. Finally, comparison of the performance of this wind profile model against existing parametric models (e.g., Holland 1980;

Willoughby et al. 2006) is a logical extension of this work for risk analysis applications. Part II explores the modes of variability inherent to the model in the case of input r_0 and their relevance to the variability of size and structure observed in nature.

Acknowledgments. This material is based upon work supported by the National Science Foundation under Awards AGS-1331362 and AGS-1032244. Very special thanks to Bryan Stiles, Svetla Hristova-Veleva, and their team at the NASA Jet Propulsion Laboratory for their help working with their excellent QuikSCAT tropical cyclone database. Thanks to Mark Donelan for sharing the drag coefficient data from his 2004 paper. We thank Mark Powell for his work developing and maintaining the HWind database. Finally, we thank three anonymous reviewers for helping to improve this work.

REFERENCES

- Abarca, S. F., and M. T. Montgomery, 2014: Are eyewall replacement cycles governed largely by axisymmetric balance dynamics? *J. Atmos. Sci.*, **71**, 3723–3738, doi:10.1175/JAS-D-14-0018.1.
- Bell, M. M., M. T. Montgomery, and K. A. Emanuel, 2012: Air–sea enthalpy and momentum exchange at major hurricane wind speeds observed during CBLAST. *J. Atmos. Sci.*, **69**, 3197–3222, doi:10.1175/JAS-D-11-0276.1.
- Bryan, G. H., and R. Rotunno, 2009: Evaluation of an analytical model for the maximum intensity of tropical cyclones. *J. Atmos. Sci.*, **66**, 3042–3060, doi:10.1175/2009JAS3038.1.
- Bu, Y. P., R. G. Fovell, and K. L. Corbosiero, 2014: Influence of cloud–radiative forcing on tropical cyclone structure. *J. Atmos. Sci.*, **71**, 1644–1662, doi:10.1175/JAS-D-13-0265.1.
- Chan, K. T., and J. C. Chan, 2012: Size and strength of tropical cyclones as inferred from QuikSCAT data. *Mon. Wea. Rev.*, **140**, 811–824, doi:10.1175/MWR-D-10-05062.1.
- , and —, 2013: Angular momentum transports and synoptic flow patterns associated with tropical cyclone size change. *Mon. Wea. Rev.*, **141**, 3985–4007, doi:10.1175/MWR-D-12-00204.1.
- Chavas, D. R., and K. A. Emanuel, 2010: A QuikSCAT climatology of tropical cyclone size. *Geophys. Res. Lett.*, **37**, 10–13, doi:10.1029/2010gl044558.
- , and K. Emanuel, 2014: Equilibrium tropical cyclone size in an idealized state of axisymmetric radiative–convective equilibrium. *J. Atmos. Sci.*, **71**, 1663–1680, doi:10.1175/JAS-D-13-0155.1.
- , and J. Vigh, 2014: QSCAT-R: The QuikSCAT tropical cyclone radial structure dataset. NCAR Tech. Note TN-513+STR, 27 pp. [Available online at <http://nldr.library.ucar.edu/repository/assets/technotes/TECH-NOTE-000-000-000-882.pdf>.]
- , and N. Lin, 2015: A model for the complete radial structure of the tropical cyclone wind field. Part II: Wind field variability. *J. Atmos. Sci.*, submitted.
- , E. Yonekura, C. Karamperidou, N. Cavanaugh, and K. Serafin, 2013: U.S. hurricanes and economic damage: An extreme value perspective. *Nat. Hazards Rev.*, **14**, 237–246, doi:10.1061/(ASCE)NH.1527-6996.0000102.
- Chen, S. S., W. Zhao, M. A. Donelan, and H. L. Tolman, 2013: Directional wind–wave coupling in fully coupled atmosphere–wave–ocean models: Results from CBLAST-Hurricane. *J. Atmos. Sci.*, **70**, 3198–3215, doi:10.1175/JAS-D-12-0157.1.

- Czajkowski, J., and J. Done, 2014: As the wind blows? Understanding hurricane damages at the local level through a case study analysis. *Wea. Climate Soc.*, **6**, 202–217, doi:10.1175/WCAS-D-13-00024.1.
- Davis, C. A., 2015: The formation of moist vortices and tropical cyclones in idealized simulations. *J. Atmos. Sci.*, doi:10.1175/JAS-D-15-0027.1, in press.
- Dean, L., K. A. Emanuel, and D. Chavas, 2009: On the size distribution of Atlantic tropical cyclones. *Geophys. Res. Lett.*, **36**, L14803, doi:10.1029/2009GL039051.
- DeMaria, M., and J. Kaplan, 1994: A Statistical Hurricane Intensity Prediction Scheme (SHIPS) for the Atlantic basin. *Wea. Forecasting*, **9**, 209–220, doi:10.1175/1520-0434(1994)009<0209:ASHIPS>2.0.CO;2.
- Didlake, A. C., and R. A. Houze, 2013a: Convective-scale variations in the inner-core rainbands of a tropical cyclone. *J. Atmos. Sci.*, **70**, 504–523, doi:10.1175/JAS-D-12-0134.1.
- , and —, 2013b: Dynamics of the stratiform sector of a tropical cyclone rainband. *J. Atmos. Sci.*, **70**, 1891–1911, doi:10.1175/JAS-D-12-0245.1.
- Donelan, M., B. Haus, N. Reul, W. Plant, M. Stiassnie, H. Graber, O. Brown, and E. Saltzman, 2004: On the limiting aerodynamic roughness of the ocean in very strong winds. *Geophys. Res. Lett.*, **31**, L18306, doi:10.1029/2004GL019460.
- Dvorak, V. F., 1984: Tropical cyclone intensity analysis using satellite data. National Oceanic and Atmospheric Administration Tech. Rep. NESDIS 11, 47 pp. [Available online at http://severe.worldweather.wmo.int/TCFW/RAI_Training/Dvorak_1984.pdf.]
- Emanuel, K. A., 1995: Sensitivity of tropical cyclones to surface exchange coefficients and a revised steady-state model incorporating eye dynamics. *J. Atmos. Sci.*, **52**, 3969–3976, doi:10.1175/1520-0469(1995)052<3969:SOTCTS>2.0.CO;2.
- , 2000: A statistical analysis of tropical cyclone intensity. *Mon. Wea. Rev.*, **128**, 1139–1152, doi:10.1175/1520-0493(2000)128<1139:ASAOTC>2.0.CO;2.
- , 2004: Tropical cyclone energetics and structure. *Atmospheric Turbulence and Mesoscale Meteorology*, E. Fedorovich, R. Rotunno, and B. Stevens, Eds., Cambridge University Press, 165–192.
- , and R. Rotunno, 2011: Self-stratification of tropical cyclone outflow. Part I: Implications for storm structure. *J. Atmos. Sci.*, **68**, 2236–2249, doi:10.1175/JAS-D-10-05024.1.
- Gopalakrishnan, S. G., F. Marks Jr., J. A. Zhang, X. Zhang, J.-W. Bao, and V. Tallapragada, 2013: A study of the impacts of vertical diffusion on the structure and intensity of the tropical cyclones using the high-resolution HWRF system. *J. Atmos. Sci.*, **70**, 524–541, doi:10.1175/JAS-D-11-0340.1.
- Holland, G. J., 1980: An analytic model of the wind and pressure profiles in hurricanes. *Mon. Wea. Rev.*, **108**, 1212–1218, doi:10.1175/1520-0493(1980)108<1212:AAMOTW>2.0.CO;2.
- , 1984: Tropical cyclone motion. A comparison of theory and observation. *J. Atmos. Sci.*, **41**, 68–75, doi:10.1175/1520-0469(1984)041<0068:TCMACO>2.0.CO;2.
- , J. I. Belanger, and A. Fritz, 2010: A revised model for radial profiles of hurricane winds. *Mon. Wea. Rev.*, **138**, 4393–4401, doi:10.1175/2010MWR3317.1.
- Irish, J. L., and D. T. Resio, 2010: A hydrodynamics-based surge scale for hurricanes. *Ocean Eng.*, **37**, 69–81, doi:10.1016/j.oceaneng.2009.07.012.
- , —, and J. J. Ratcliff, 2008: The influence of storm size on hurricane surge. *J. Phys. Oceanogr.*, **38**, 2003–2013, doi:10.1175/2008JPO3727.1.
- Jelesnianski, C. P., 1966: Numerical computations of storm surges without bottom stress. *Mon. Wea. Rev.*, **94**, 379–394, doi:10.1175/1520-0493(1966)094<0379:NCOSSW>2.3.CO;2.
- Keper, J. D., 2010: Slab- and height-resolving models of the tropical cyclone boundary layer. Part I: Comparing the simulations. *Quart. J. Roy. Meteor. Soc.*, **136**, 1686–1699, doi:10.1002/qj.667.
- , 2013: How does the boundary layer contribute to eyewall replacement cycles in axisymmetric tropical cyclones? *J. Atmos. Sci.*, **70**, 2808–2830, doi:10.1175/JAS-D-13-046.1.
- Knaff, J. A., and R. M. Zehr, 2007: Reexamination of tropical cyclone wind–pressure relationships. *Wea. Forecasting*, **22**, 71–88, doi:10.1175/WAF965.1.
- , J. P. Kossin, and M. DeMaria, 2003: Annular hurricanes. *Wea. Forecasting*, **18**, 204–223, doi:10.1175/1520-0434(2003)018<0204:AH>2.0.CO;2.
- , S. P. Longmore, and D. A. Molenaar, 2014: An objective satellite-based tropical cyclone size climatology. *J. Climate*, **27**, 455–476, doi:10.1175/JCLI-D-13-00096.1.
- Lin, N., and D. Chavas, 2012: On hurricane parametric wind and applications in storm surge modeling. *J. Geophys. Res.*, **117**, D09120, doi:10.1029/2011JD017126.
- , K. Emanuel, M. Oppenheimer, and E. Vanmarcke, 2012: Physically based assessment of hurricane surge threat under climate change. *Nat. Climate Change*, **2**, 462–467, doi:10.1038/nclimate1389.
- Liu, K. S., and J. C. L. Chan, 1999: Size of tropical cyclones as inferred from ERS-1 and ERS-2 data. *Mon. Wea. Rev.*, **127**, 2992–3001, doi:10.1175/1520-0493(1999)127<2992:SOTCAI>2.0.CO;2.
- Merrill, R. T., 1984: A comparison of large and small tropical cyclones. *Mon. Wea. Rev.*, **112**, 1408–1418, doi:10.1175/1520-0493(1984)112<1408:ACOLAS>2.0.CO;2.
- Molinari, J., and D. Vollaro, 2014: Symmetric instability in the outflow layer of a major hurricane. *J. Atmos. Sci.*, **71**, 3739–3746, doi:10.1175/JAS-D-14-0117.1.
- , P. Duran, and D. Vollaro, 2014: Low Richardson number in the tropical cyclone outflow layer. *J. Atmos. Sci.*, **71**, 3164–3179, doi:10.1175/JAS-D-14-0005.1.
- Potter, H., H. C. Graber, N. J. Williams, C. O. Collins III, R. J. Ramos, and W. M. Drennan, 2015: In situ measurements of momentum fluxes in typhoons. *J. Atmos. Sci.*, **72**, 104–118, doi:10.1175/JAS-D-14-0025.1.
- Powell, M. D., S. H. Houston, L. R. Amat, and N. Morisseau-Leroy, 1998: The HRD real-time hurricane wind analysis system. *J. Wind Eng. Ind. Aerodyn.*, **77–78**, 53–64, doi:10.1016/S0167-6105(98)00131-7.
- , P. J. Vickery, and T. A. Reinhold, 2003: Reduced drag coefficient for high wind speeds in tropical cyclones. *Nature*, **422**, 279–283, doi:10.1038/nature01481.
- Reasor, P. D., M. T. Montgomery, F. D. Marks Jr., and J. F. Gamache, 2000: Low-wavenumber structure and evolution of the hurricane inner core observed by airborne dual-Doppler radar. *Mon. Wea. Rev.*, **128**, 1653–1680, doi:10.1175/1520-0493(2000)128<1653:LWSAEO>2.0.CO;2.
- Richter, D. H., and D. P. Stern, 2014: Evidence of spray-mediated air-sea enthalpy flux within tropical cyclones. *Geophys. Res. Lett.*, **41**, 2997–3003, doi:10.1002/2014GL059746.
- Rotunno, R., and G. H. Bryan, 2012: Effects of parameterized diffusion on simulated hurricanes. *J. Atmos. Sci.*, **69**, 2284–2299, doi:10.1175/JAS-D-11-0204.1.
- Sanger, N. T., M. T. Montgomery, R. K. Smith, and M. M. Bell, 2014: An observational study of tropical cyclone

- spinup in Supertyphoon Jangmi (2008) from 24 to 27 September. *Mon. Wea. Rev.*, **142**, 3–28, doi:10.1175/MWR-D-12-00306.1.
- Smith, R. K., 1980: Tropical cyclone eye dynamics. *J. Atmos. Sci.*, **37**, 1227–1232, doi:10.1175/1520-0469(1980)037<1227:TCED>2.0.CO;2.
- , and M. T. Montgomery, 2008: Balanced boundary layers used in hurricane models. *Quart. J. Roy. Meteor. Soc.*, **134**, 1385–1395, doi:10.1002/qj.296.
- Sobel, A. H., and C. S. Bretherton, 2000: Modeling tropical precipitation in a single column. *J. Climate*, **13**, 4378–4392, doi:10.1175/1520-0442(2000)013<4378:MTPIAS>2.0.CO;2.
- Stern, D. P., and D. S. Nolan, 2011: On the vertical decay rate of the maximum tangential winds in tropical cyclones. *J. Atmos. Sci.*, **68**, 2073–2094, doi:10.1175/2011JAS3682.1.
- , J. R. Brisbois, and D. S. Nolan, 2014: An expanded dataset of hurricane eyewall sizes and slopes. *J. Atmos. Sci.*, **71**, 2747–2762, doi:10.1175/JAS-D-13-0302.1.
- Tang, B., and K. Emanuel, 2010: Midlevel ventilation's constraint on tropical cyclone intensity. *J. Atmos. Sci.*, **67**, 1817–1830, doi:10.1175/2010JAS3318.1.
- , and —, 2012: A ventilation index for tropical cyclones. *Bull. Amer. Meteor. Soc.*, **93**, 1901–1912, doi:10.1175/BAMS-D-11-00165.1.
- Tobin, I., S. Bony, and R. Roca, 2012: Observational evidence for relationships between the degree of aggregation of deep convection, water vapor, surface fluxes, and radiation. *J. Climate*, **25**, 6885–6904, doi:10.1175/JCLI-D-11-00258.1.
- Uhlhorn, E. W., B. W. Klotz, T. Vukicevic, P. D. Reasor, and R. F. Rogers, 2014: Observed hurricane wind speed asymmetries and relationships to motion and environmental shear. *Mon. Wea. Rev.*, **142**, 1290–1311, doi:10.1175/MWR-D-13-00249.1.
- Weatherford, C., and W. Gray, 1988: Typhoon structure as revealed by aircraft reconnaissance. Part I: Data analysis and climatology. *Mon. Wea. Rev.*, **116**, 1032–1043, doi:10.1175/1520-0493(1988)116<1032:TSARBA>2.0.CO;2.
- Willoughby, H., R. Darling, and M. Rahn, 2006: Parametric representation of the primary hurricane vortex. Part II: A new family of sectionally continuous profiles. *Mon. Wea. Rev.*, **134**, 1102–1120, doi:10.1175/MWR3106.1.
- Wing, A. A., and K. A. Emanuel, 2014: Physical mechanisms controlling self-aggregation of convection in idealized numerical modeling simulations. *J. Adv. Model. Earth Syst.*, **6**, 59–74, doi:10.1002/2013MS000269.
- Xu, J., and Y. Wang, 2010: Sensitivity of the simulated tropical cyclone inner-core size to the initial vortex size. *Mon. Wea. Rev.*, **138**, 4135–4157, doi:10.1175/2010MWR3335.1.
- Zweers, N., V. Makin, J. de Vries, and V. Kudryavtsev, 2015: The impact of spray-mediated enhanced enthalpy and reduced drag coefficients in the modelling of tropical cyclones. *Bound.-Layer Meteor.*, **155**, 501–514, doi:10.1007/s10546-014-9996-1.